Supplement of “Large autumn heterotrophic respiration signal across northeast Eurasia”

Brendan Byrne[1], Junjie Liu[1,2], Yonghong Yi[3,4], Abhishek Chatterjee[1,5,6], Sourish Basu[6,7], Rui Cheng[2], Russell Doughty[2,8], Frédéric Chevallier[9], Kevin W. Bowman[1,3], Nicholas C. Parazoo[1], David Crisp[1], Xing Li[10], Jingfeng Xiao[11], Stephen Sitch[12], Bertrand Guenet[13], Feng Deng[14], Matthew S. Johnson[15], Patrick C. McGuire[16], and Charles E. Miller[1]

[1]Jet Propulsion Laboratory, California Institute of Technology, Pasadena, CA, USA
[2]Division of Geological and Planetary Sciences, California Institute of Technology, Pasadena, CA, USA
[3]Joint Institute for Regional Earth System Science and Engineering, University of California, Los Angeles, CA, USA
[4]College of Surveying and Geo-Informatics, Tongji University, China
[5]Universities Space Research Association, Columbia, MD, USA
[6]Global Modeling and Assimilation Office, NASA Goddard Space Flight Center, Greenbelt, MD, USA
[7]Earth System Science Interdisciplinary Center, University of Maryland, College Park, MD, USA
[8]College of Atmospheric and Geographic Sciences, University of Oklahoma, Norman, OK USA
[9]Laboratoire des Sciences du Climat et de l’Environnement/IPSL, CEA-CNRS-UVSQ, Université Paris-Saclay, 91191 Gif-sur-Yvette, France
[10]Research Institute of Agriculture and Life Sciences, Seoul National University, Seoul, South Korea
[11]Earth Systems Research Center, Institute for the Study of Earth, Oceans, and Space, University of New Hampshire, Durham, NH, USA
[12]College of Life and Environmental Sciences, University of Exeter, Exeter EX4 4RJ, UK
[13]Laboratoire de Géologie, Ecole Normale Supérieure/CNRS UMR8538, IPSL, PSL Research University, Paris, France
[14]Department of Physics, University of Toronto, Toronto, Ontario, Canada
[15]NASA Ames Research Center, Moffett Field, CA, USA
[16]Department of Meteorology and National Centre for Atmospheric Science, University of Reading, Reading, UK

Correspondence: Brendan Byrne (brendan.k.byrne@jpl.nasa.gov)

1 Introduction

This supporting information contains two supporting text sections, 18 supporting figures and one supporting table.

Text S1. Evaluation of CMS-Flux$_{14\mathrm{day}}$ inversion against aircraft data

Independent CO_2 measurements are sparse over northern Eurasia, particularly over the northeastern region. Therefore, we examine airborne CO_2 measurements in the free troposphere over Alaska to investigate the accuracy of the seasonal cycle estimate by the CMS-Flux$_{14\mathrm{day}}$ flux inversions. Previous analyses have shown that CO_2 measurements over Alaska are sensitive to surface fluxes over northern Eurasia (see Fig. S5 of Byrne et al. (2020)).

Before comparing to airborne CO_2 measurements, we first show that the CMS-Flux$_{14\mathrm{day}}$ NEE estimates are in family with those of the OCO-2 MIPv9 flux inversions. Figure S10 shows the CMS-Flux$_{14\mathrm{day}}$ inversions aggregated to monthly resolution (mean of 2015, 2016, 2018 and 2019). These inversions show good agreement with the MIPv9 ensembles and generally fall within the interquartile range. The largest differences occur for the IS inversions that shows reduced May–June uptake relative to the MIPv9 ensemble in the Warm and Mid regions. Nevertheless, this plot shows that the inversions largely capture the same features of the MIPv9 flux inversions relative to the prior ensemble. Figure S11 shows the CMS-Flux$_{14\mathrm{day}}$ NEE fluxes over the cold region and comparison with aircraft measurements over Alaska. For this comparison we sample the posterior CO_2 fields at the same time and altitude that airborne measurements occur. We include airborne measurements between 3000 m and 8000 m above the model surface over the domain 55°–90° N and 130°–180° W during the years 2015, 2016, 2018 and 2019. We calculate the monthly averages across these four years. We find that all flux inversions perform well in capturing the seasonal cycle of airborne CO_2 measurements relative to the prior. This comparison provides further evidence that strong summer uptake and autumn release of CO_2 occurs over northeastern Eurasia. Interestingly, the posterior fluxes still appear to underestimate the strength of the summer uptake (all CMS-Flux$_{14\mathrm{day}}$ inversions overestimate the observed CO_2 during July) and underestimate the release during the autumn (all CMS-Flux$_{14\mathrm{day}}$ inversions underestimate CO_2 during October).

Text S2. Evaluation of MERRA-2 Land T_{soil}

A key result of the analysis is that a delayed seasonal peak in soil temperature with depth is suggestive of a substantial R_h signal at depth. Here, we confirm that the seasonal cycle of MERRA-2 soil temperature with depth is consistent with observational constraints from borehole measurements, and regional simulations from ERA5 and CMIP6.

Figure S13 shows a comparison of MERRA-2 Land soil temperature and borehole measurements downloaded from the Global Terrestrial Network for Permafrost (GTN-P) over two depth intervals. We examine data from the following sites: Anderson, Anaktuvuk Pass, Ambler, Arctic Village, Barentsburg Borehole 2, Bayelva Ny Alesund, Banks Island Dataset 1349, Banks Island Dataset 1348, Deadhorse 1, Deadhorse 2, Chandalar Shelf, Bonanza Creek, Bonanza Creek 2, Endalen PYRN, College Peat, Kapp Linne 1, Kapp Linne 2, Happy Valley 1 b, Happy Valley 1 ib, Gakona 2, Galbraith Lake, Ivotuk 4 Dataset 820, Ivotuk 4 Dataset 819, Ivotuk 3 Dataset 814, ILU2007, Franklin Bluffs wet b Dataset 666, Franklin Bluffs surface Dataset 660, Franklin Bluffs dry ib Dataset 665, Franklin Bluffs dry be Dataset 664, Franklin Bluffs dry b Dataset 663, Franklin Bluffs dry b Dataset 35, Lake Elgygytgyn, Kashin 01k, Last Bridge, NGTS UNIS east, Nadym ND3 4, Nadym ND3, Nadym ND2, Old Auroral Station PYRN, Mary's Igloo East, Mould Bay Dataset 1355, Mould Bay Dataset 1354, Peski 1 Dataset 1406, Salmon Lake, Piz Bo, Smith Lake 2, Smith Lake 3, Smith Lake 4, and West Dock 1 surface Dataset 615.

The seasonal peak in soil temperature from MERRA-2 well reproduces the borehole soil temperature peak for the 0–50 cm and 50–200 cm depth intervals, and accurately captures the phase shift in temperature. The largest data-model differences occur during the winter (Dec–Mar), where the MERRA-2 soil temperature is biased 2–3 °C high. This bias could be partially inpacted by differences in the time periods examined. We average the seasonal cycle in borehole data for all available measurements over 1998–2020, whereas we examine the 2015–2018 period for the MERRA-2 data, so it is possible that climate warming could impact the inferred bias.

Figure S14 shows the regional simulated seasonal cycle of soil temperature over four depth intervals for MERRA-2 Land (2015–2019), ERA5 Land (2015–2019), and seven CMIP6 models (2010–2019). For the CMIP6, models we examine the median and interquartile range across the mean seasonal cycles over 2010–2019. All of the model estimates show close agreement in the seasonality of soil temperature across the regions with depth. Each model captures a similar phase shift in soil temperature with depth. The largest differences are evident in the Cold region, particularly during the winter, where MERRA-2 is about $\sim$5 °C colder than ERA5 (and the CMIP6 models largely fall in between). Interestingly, the MERRA-2 Land reanalysis showed the opposite (warm) bias relative to the borehole data. Nevertheless, this comparison shows that the MERRA-2 Land soil temperature is in good agreement with borehole measurements and other models in simulating the seasonal cycle of soil temperature at high latitudes.

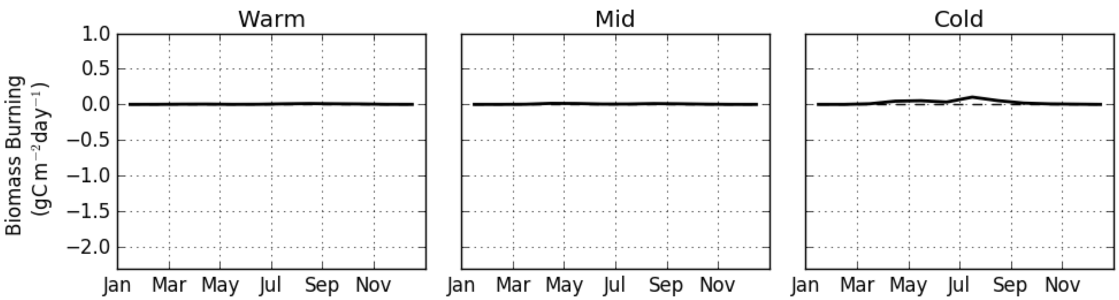

Figure S1. GFED4.1 Biomass burning emissions of CO_2.

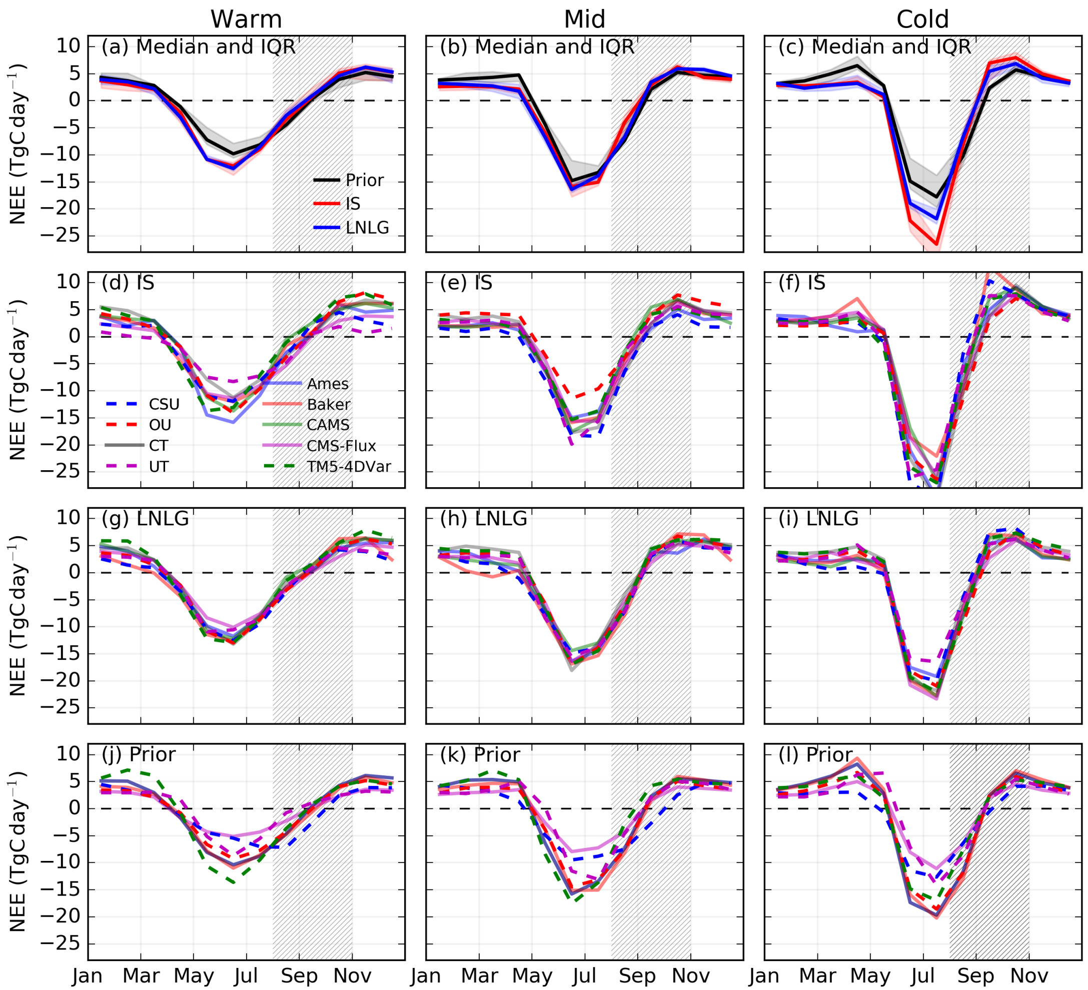

Figure S2. NEE fluxes from individual MIPv9 participants. (a-c) Median and interquartile spread for each experiment. Individual model NEE estimates for the (d-f) IS experiment, (g-i) LNLG experiment, and (j-l) prior fluxes.

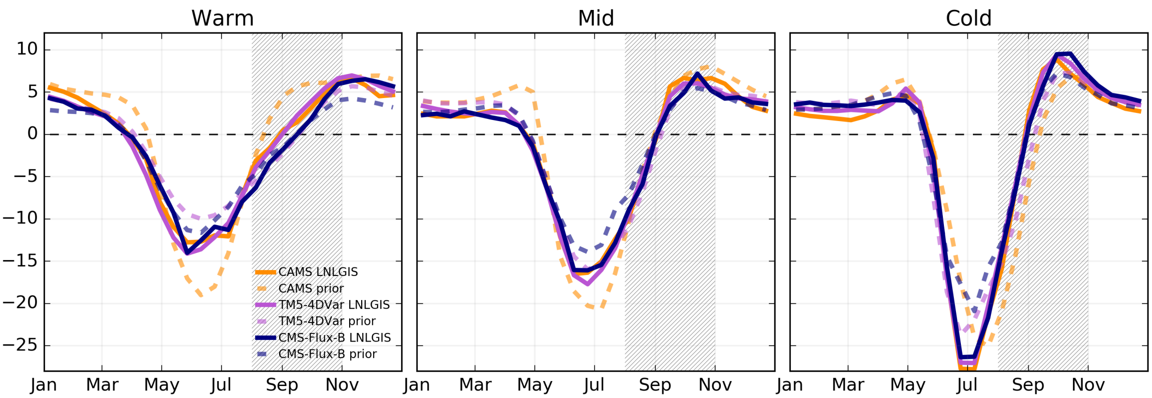

Figure S3. Prior (dashed) and posterior (solid) NEE fluxes at 14 day temporal resolution for CAMS$_{14\mathrm{day}}$ (orange), TM5-4DVar$_{14\mathrm{day}}$ (magenta), and CMS-Flux$_{14\mathrm{day}}$ (navy blue) flux inversions.

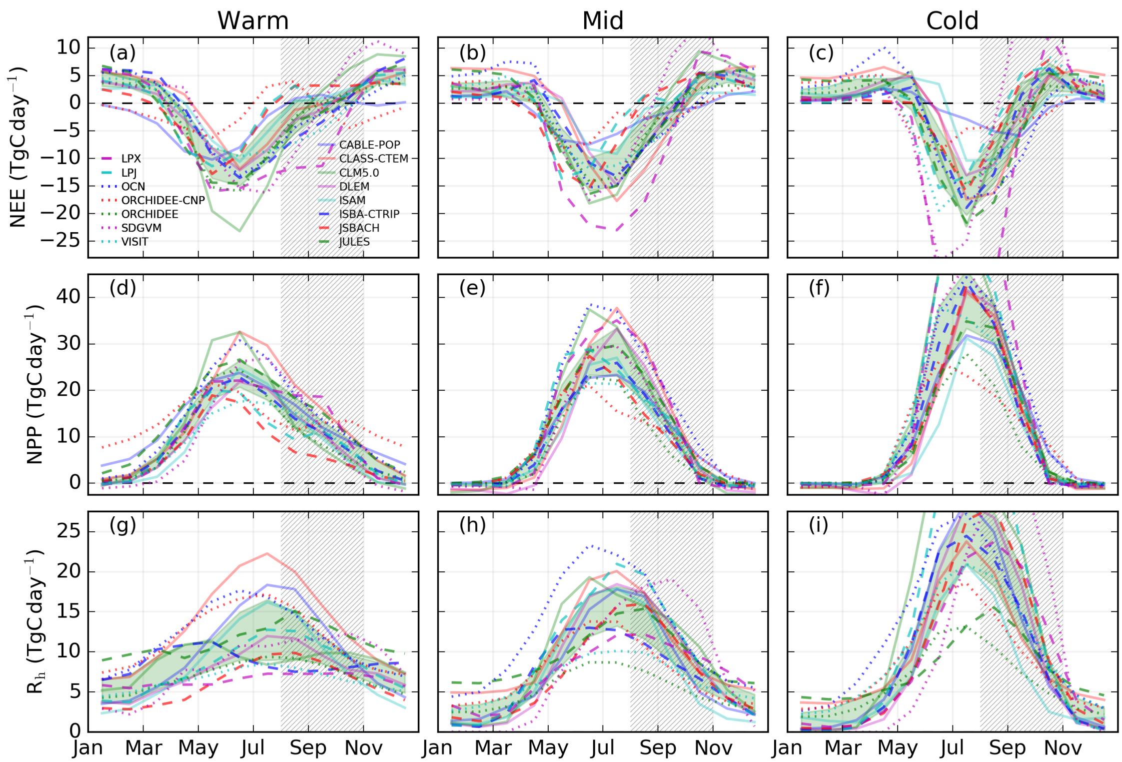

Figure S4. (a-c) NEE, (d-f) NPP, and (g-i) $\mathrm{R_h}$ seasonal cycles simulated by each TRENDY v8 model examined in this study. The shaded green area shows the TRENDY model interquartile spread, while individual lines show specific models: (dash magenta) LPX, (dashed cyan) LPJ, (dotted blue) OCN, (dotted red) ORCHIDEE-CNP, (dotted green) ORCHIDEE, (dotted magenta) SDGVM, (dotted cyan) VISIT, (solid blue) CABLE-POP, (solid red) CLASS-CTEM, (solid green) CLM5.0, (solid magenta) DLEM, (solid cyan) ISAM, (dashed blue) ISBA-CTRIP, (dashed red) JSBACH, and (dashed green) JULES.

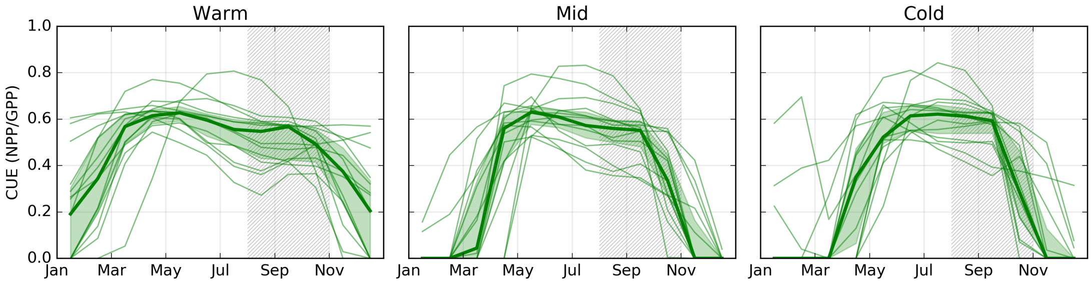

Figure S5. CUE (NPP/GPP) for the TRENDY models. Thin green lines show the CUE for individual models while the thick green line shows the median and shaded regions shows the interquartile spread.

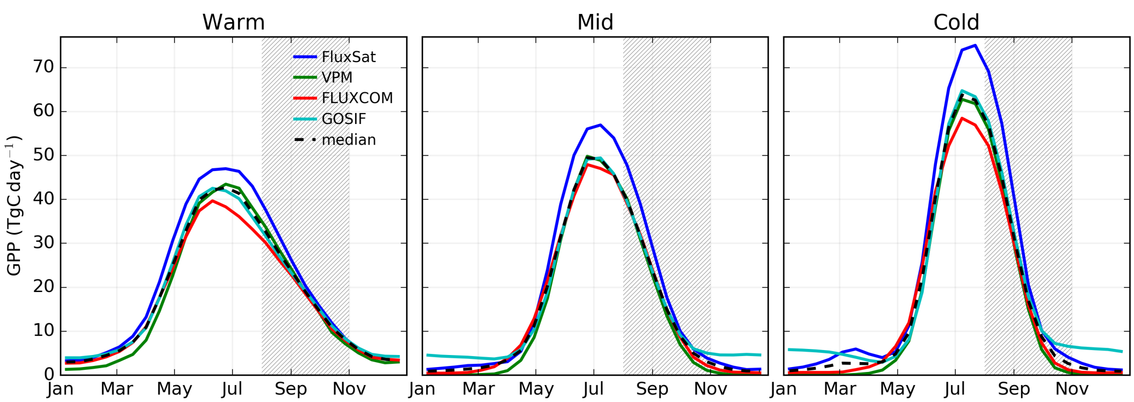

Figure S6. GPP fluxes at 14 day temporal resolution from FluxSat (blue), VPM (green), FLUXCOM (red), and GOSIF (cyan).

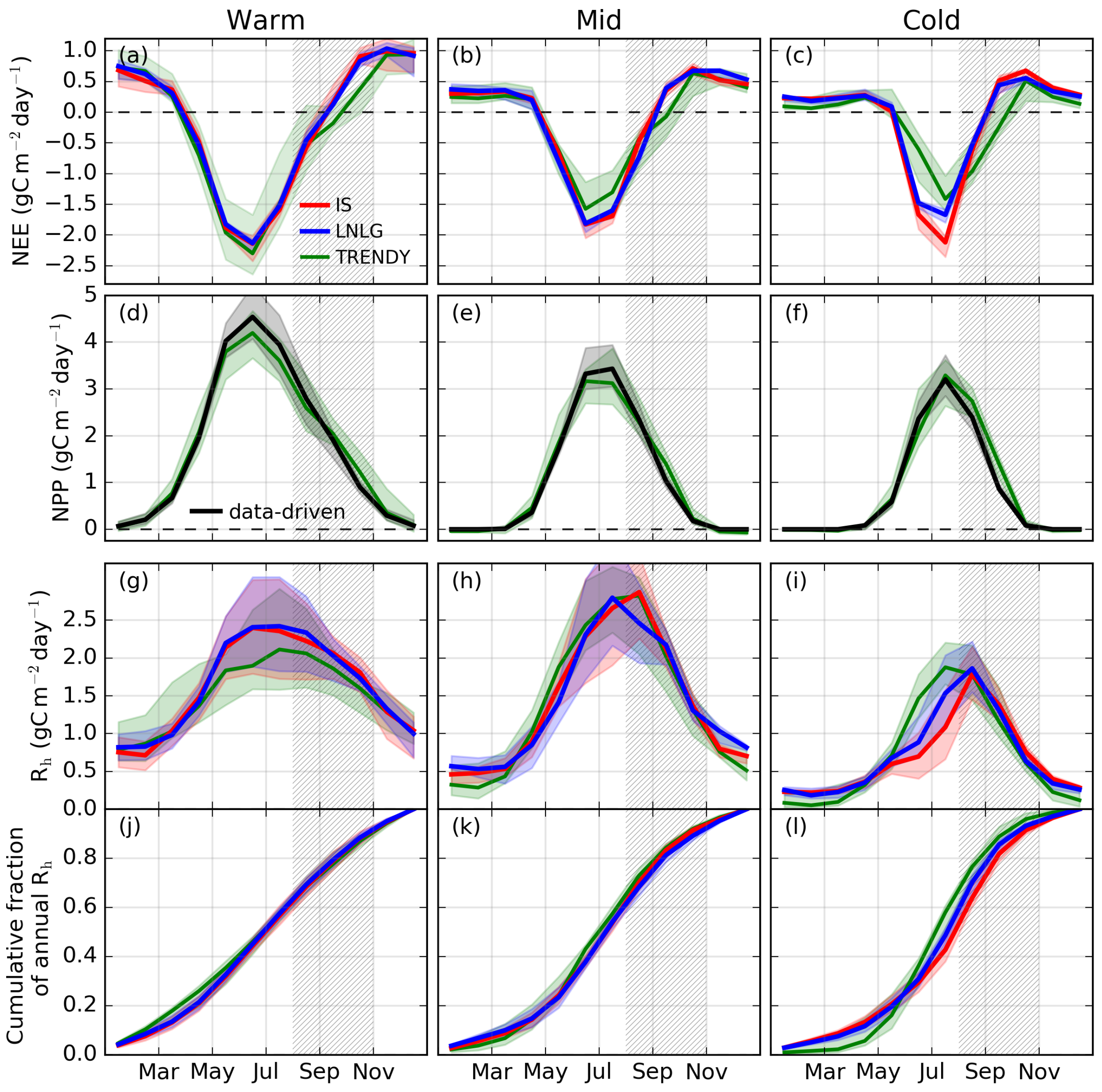

Figure S7. Same as Fig. 2 of main text but with units in $\mathrm{gC\,m^{-2}\,day^{-1}}$ rather than $\mathrm{TgC\,day^{-1}}$.

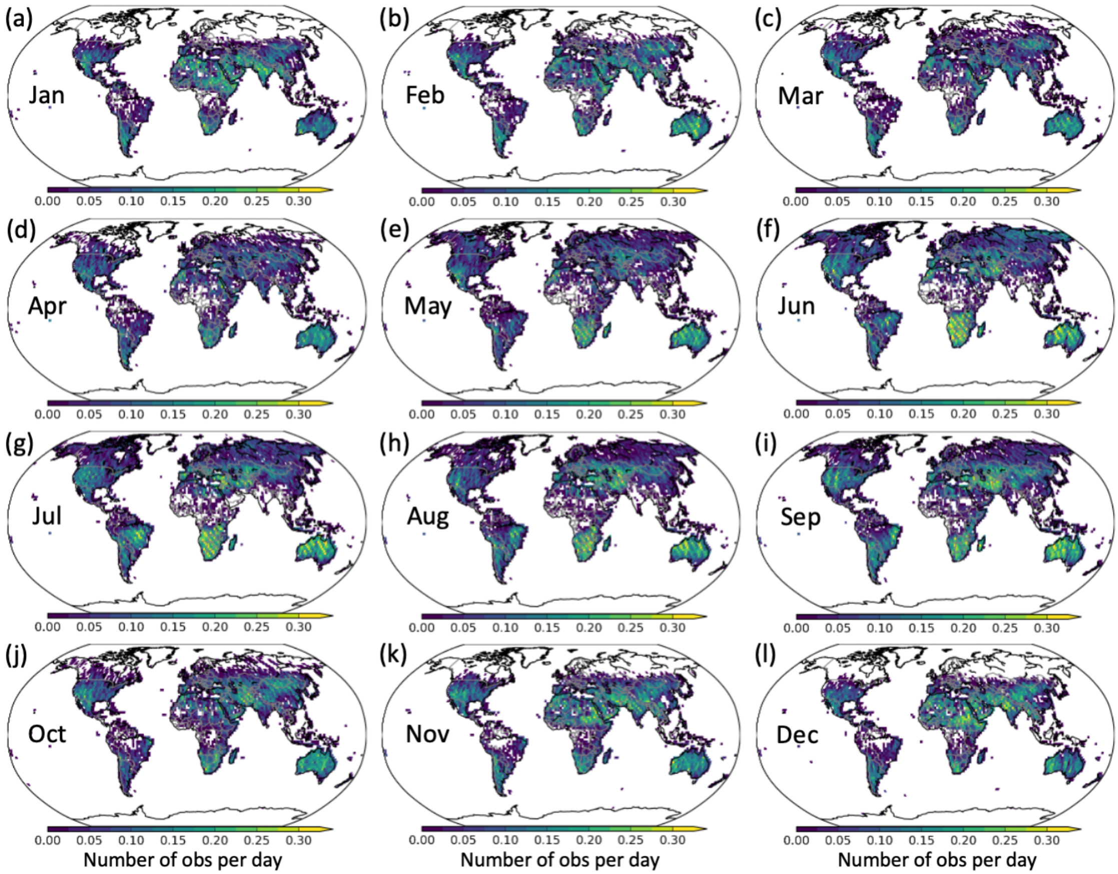

Figure S8. Spatial coverage of monthly OCO-2 land X_{CO_2} retrievals averaged over four years (2015, 2016, 2018, and 2019). (a-l) Monthly mean observations per day of OCO-2 ACOS v10 combined land nadir and land glint 10 sec X_{CO_2} super-obs on a $1^\circ \times 1^\circ$ spatial grid.

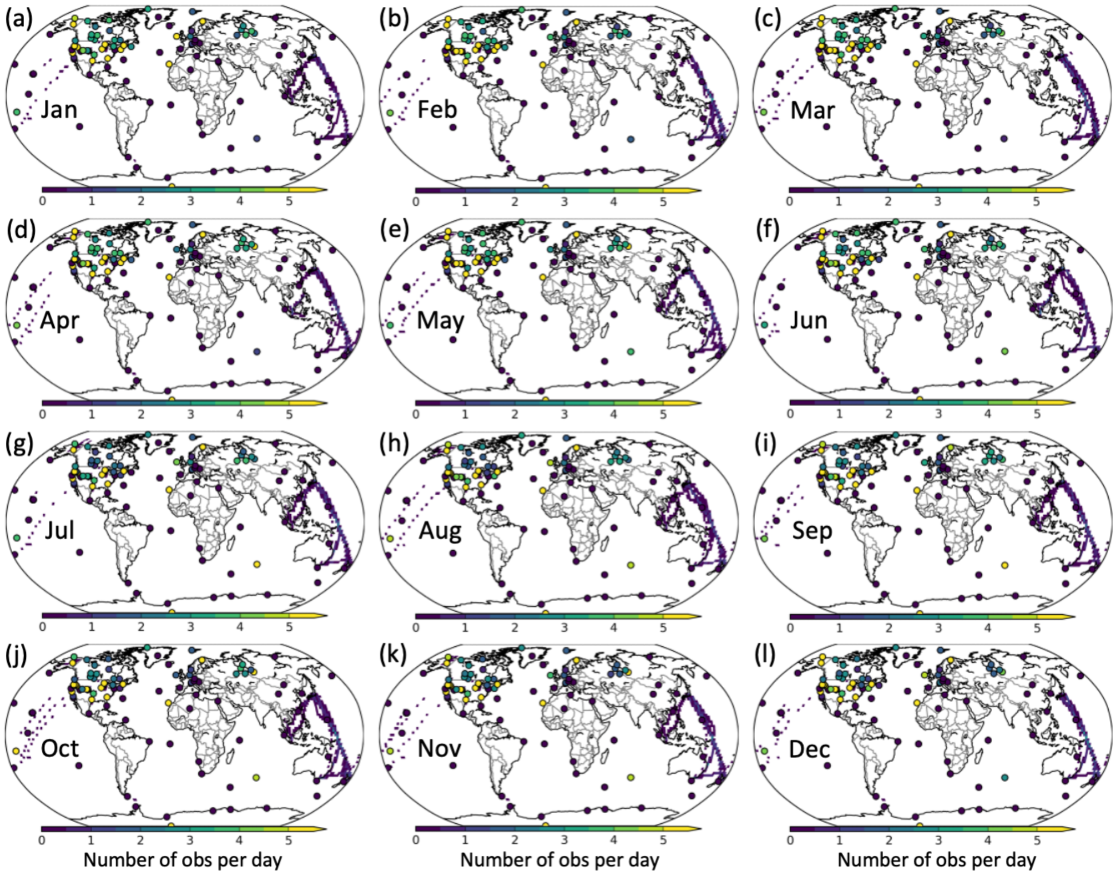

Figure S9. Spatial coverage of monthly in situ and flask measurements averaged over four years (2015, 2016, 2018, and 2019). (a-l) Monthly mean observations per day assimilated in to OCO-2 v10 MIP. Sites are shown by circles while shipboard and aircraft measurements are aggregated to a $1^\circ \times 1^\circ$ spatial grid.

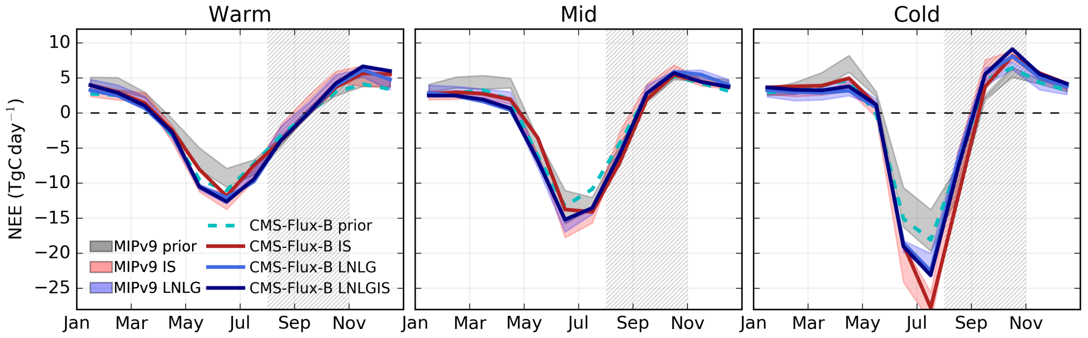

Figure S10. Seasonal cycle of NEE for the OCO-2 MIPv9 and CMS-Flux$_{14\mathrm{day}}$ flux inversions at monthly temporal resolution over the (a) warm, (b) mid, and (c) cold regions. The shaded regions show the interquartile spread for the MIPv9 prior (grey), IS (red) and LNLG (blue) ensembles. The lines show the CMS-Flux$_{14\mathrm{day}}$ prior (dashed cyan), IS (red), LNLG (blue), and LNLGIS (navy).

Table 1. Site name, latitude, longitude and vegetation type for the FLUXNET sites examined in this study.

Site	Lat	Lon	vegetation type
CA-Man	55.8796	-98.4808	Evergreen Needleleaf Forests
CA-NS1	55.8792	-98.4839	Evergreen Needleleaf Forests
CA-NS2	55.9058	-98.5247	Evergreen Needleleaf Forests
CA-NS3	55.9117	-98.3822	Evergreen Needleleaf Forests
CA-NS4	55.9144	-98.3806	Evergreen Needleleaf Forests
CA-NS5	55.8631	-98.4850	Evergreen Needleleaf Forests
CA-NS6	55.9167	-98.9644	Open Shrublands
CA-NS7	56.6358	-99.9483	Open Shrublands
CA-SF3	54.0916	-106.0053	Open Shrublands
FI-Lom	67.9972	24.2092	Permanent Wetlands
FI-Sod	67.3624	26.6386	Evergreen Needleleaf Forests
RU-Che	68.6130	161.3414	Permanent Wetlands
RU-Cok	70.8291	147.4943	Open Shrublands
RU-Ha1	54.7252	90.0022	Grasslands
US-Prr	65.1237	-147.4876	Evergreen Needleleaf Forests

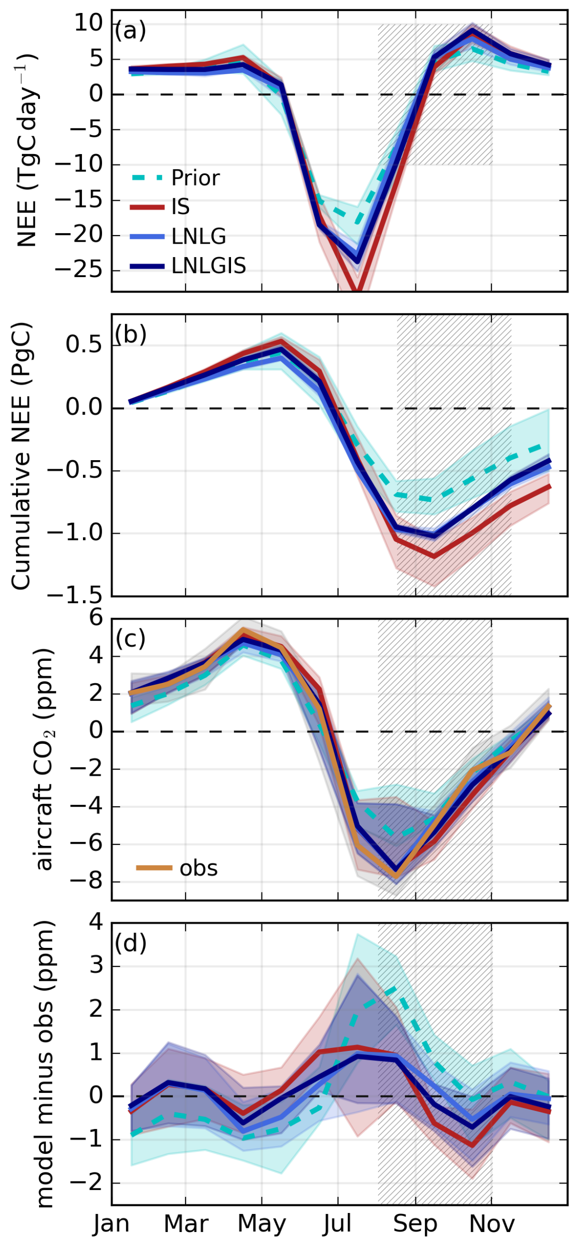

Figure S11. Comparison of flux inversions and aircraft CO_2 measurements over Alaska. (a) Prior (dashed) and LNLGIS (solid) monthly NEE over the cold region. Shaded areas show the range from the three prior NEE estimates employed in the CMS-Flux$_{14\mathrm{day}}$ inversions. (b) Cumulative NEE CO_2 flux since the beginning of the year. (c) Mean observed (brown) and simulated atmospheric CO_2 seasonal cycle for airborne measurements over Alaska. (d) Monthly mean simulated CO_2 measurements minus the observations over Alaska.

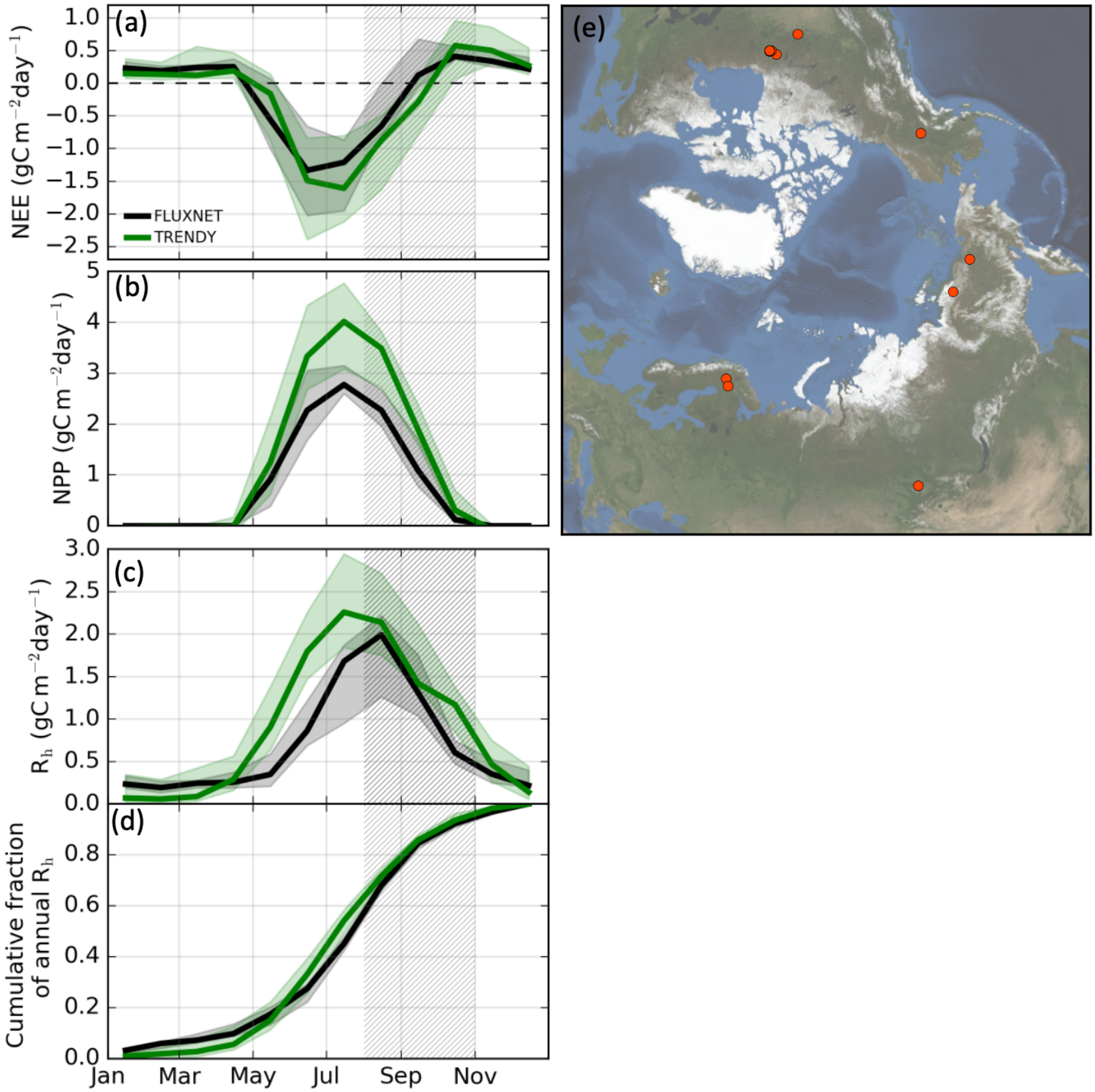

Figure S12. Median and interquartile spread in carbon fluxes measured (black) and simulated by TRENDY (green) at 15 FLUXNET sites. Mean seasonal cycles are shown for (a) NEE, (b) NPP, (c) R_h, and (d) cumulative fraction of R_h measured (black). (e) Location of 15 high-latitude FLUXNET sites in regions with the mean October air temperatures less than 2°C.

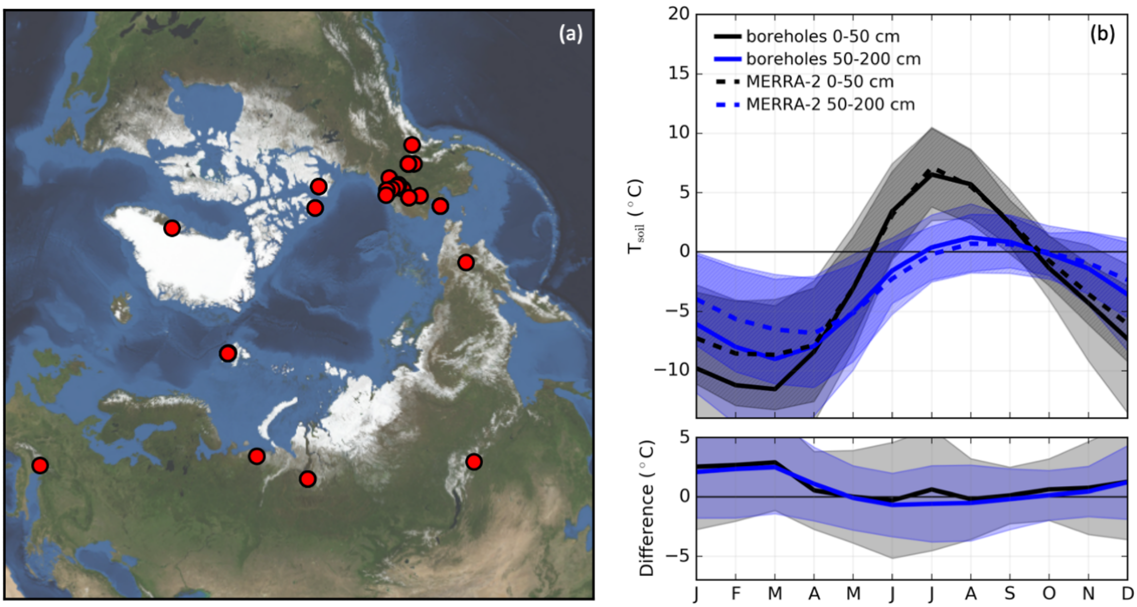

Figure S13. Comparison of MERRA-2 Land soil temperature to borehole measurements over 1998–2020. (a) locations of borehole temperature measurement sites. (b) Mean seasonal cycle of borehole temperature with shading showing one standard deviation across the sites. MERRA-2 Land soil temperatures (mean over 2015-2018) sampled at the model grids containing the boreholes.

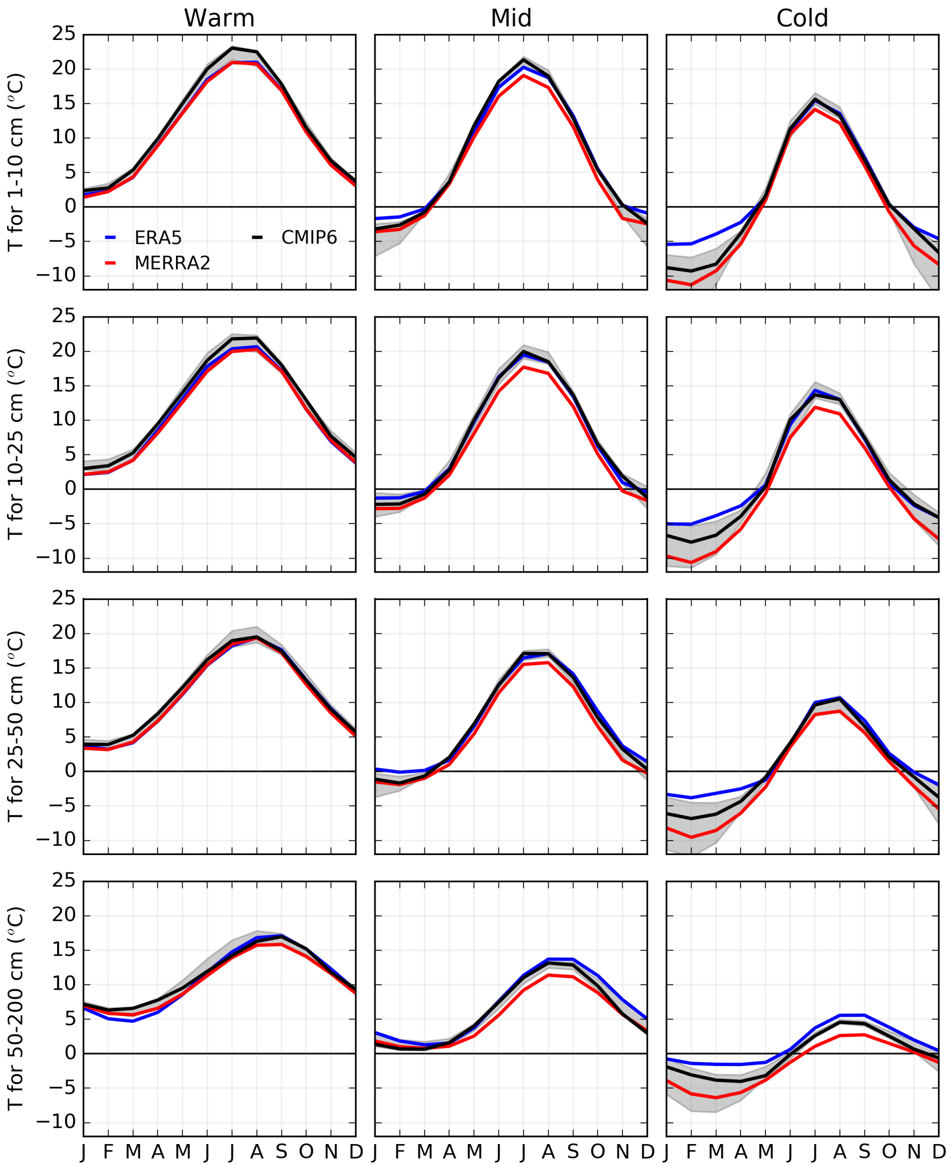

Figure S14. Seasonal cycle of soil temperature for three regions and four different depth intervals (1–10 cm, 10–25 cm, 25–50 cm, 50–200 cm) estimated by MERRA-2 Land, ERA5 Land, and CMIP6 models. MERRA-2 (red) and ERA5 (blue) seasonal cycles are calculated as the mean over 2010–2019. For CMIP6, the mean seasonal cycle over 2010–2019 is calculated for each model, then the model median (solid black) and interquatile range (shaded grey) are plotted across the seven models included in this analysis.

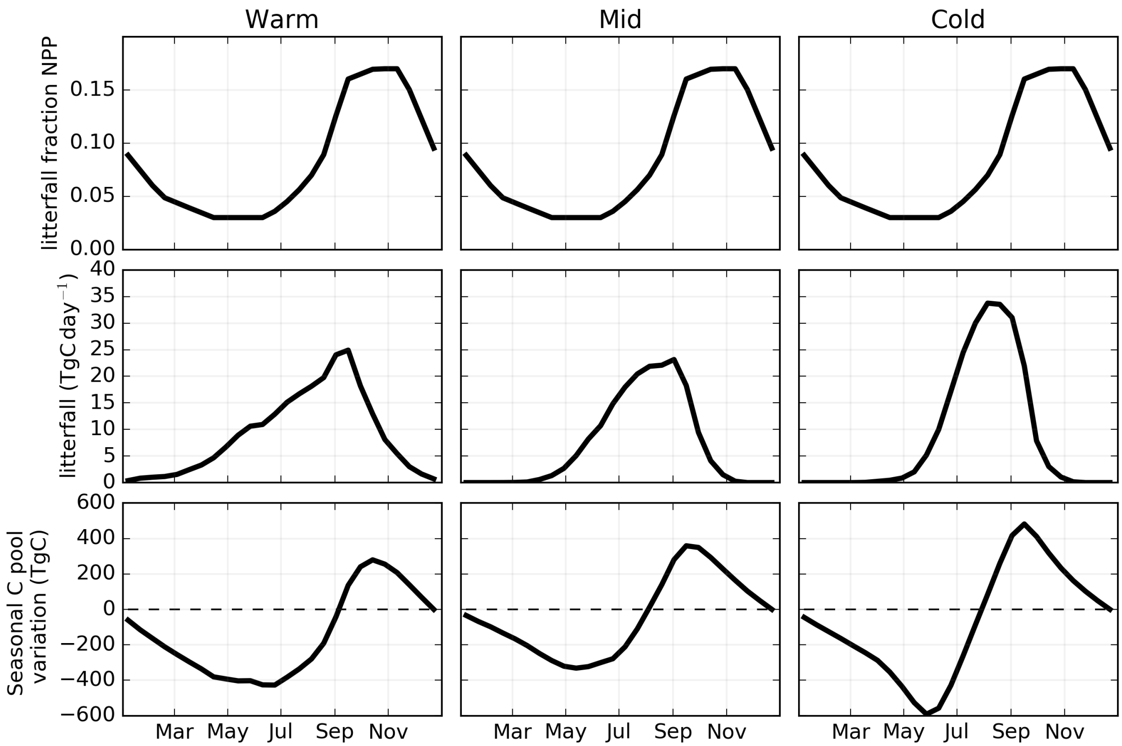

Figure S15. (top) Fraction of NPP that becomes litterfall. (middle row) Carbon flux from litterall. (bottom) Seasonal variations in the labile carbon pool due to litterfall and $\mathrm{R_h}$.

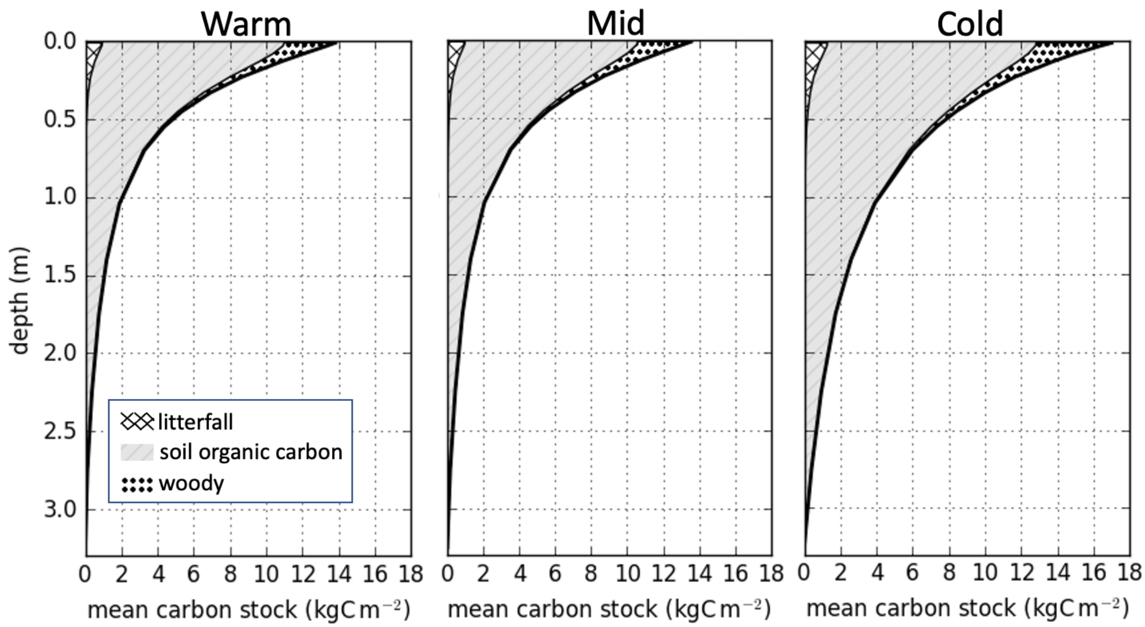

Figure S16. Regional carbon stocks with depth simulated by the soil carbon decomposition model

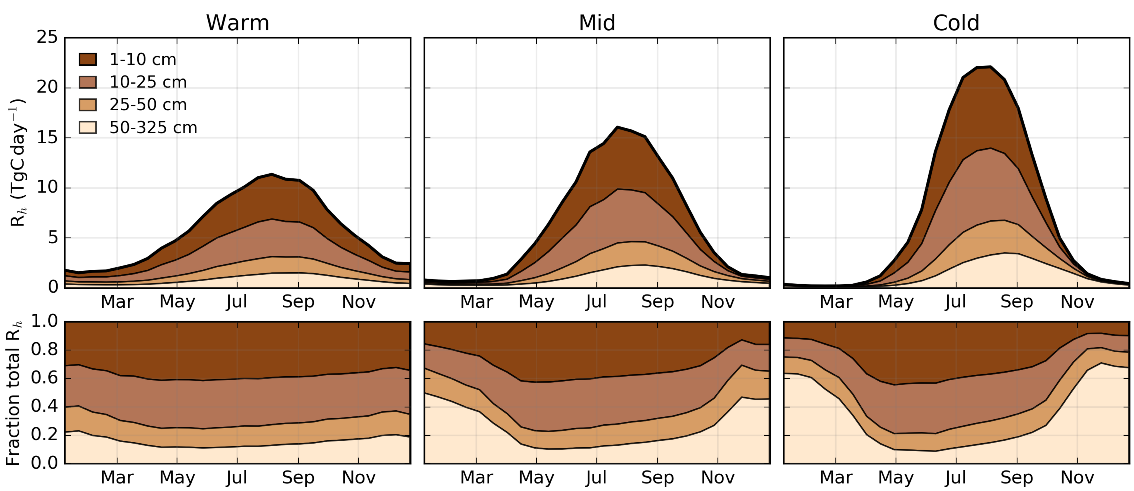

Figure S17. Seasonal cycle of R$_h$ from four soil carbon layers simulated by the soil carbon decomposition model.

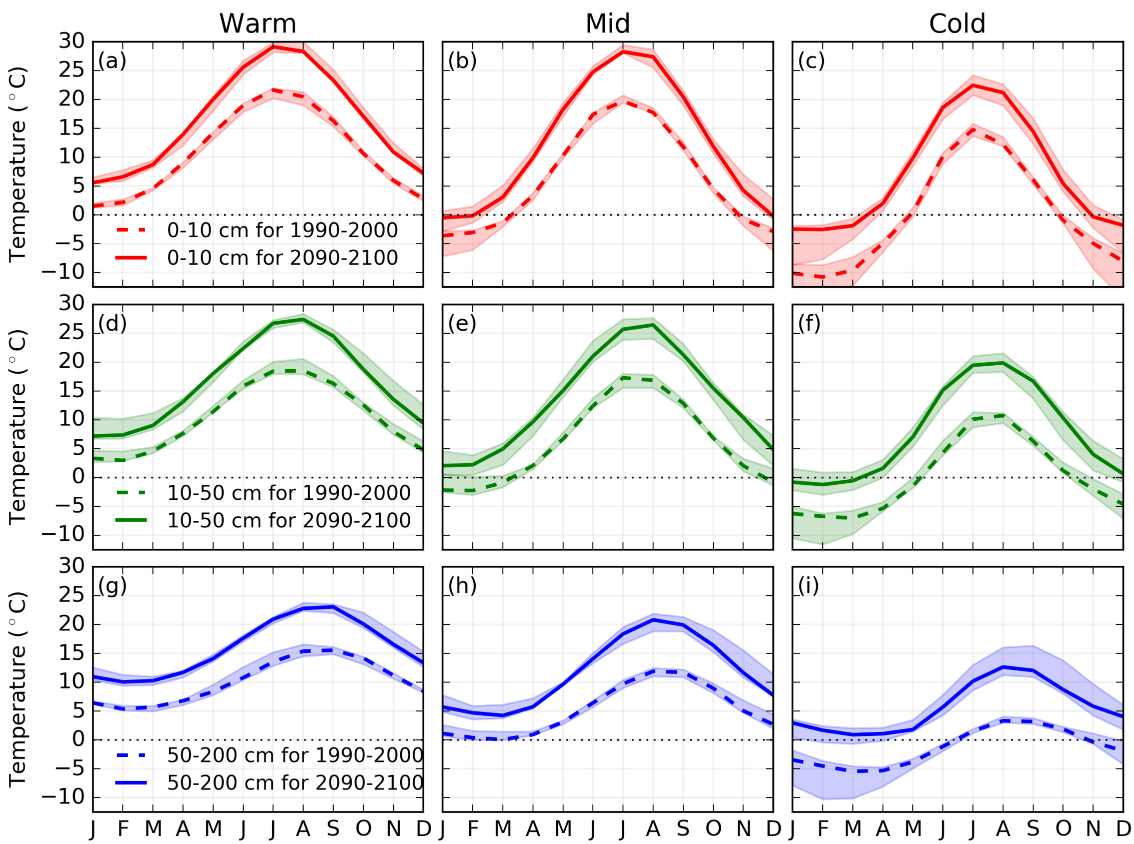

Figure S18. Simulated soil surface temperature for 1990–2000 (dashed) and 2090-2100 (solid) averaged over depths of (a-c) 0–10 cm, (d-f) 10-50 cm and (g-i) 50–200 cm for the three Eurasian regions examined in this study. The lines show the model median and shaded area shows the interquartile spread.

References

Byrne, B., Liu, J., Lee, M., Baker, I. T., Bowman, K. W., Deutscher, N. M., Feist, D. G., Griffith, D. W., Iraci, L. T., Kiel, M., Kimball, J., Miller, C. E., Morino, I., Parazoo, N. C., Petri, C., Roehl, C. M., Sha, M., Strong, K., Velazco, V. A., Wennberg, P. O., and Wunch, D.: Improved constraints on northern extratropical CO_2 fluxes obtained by combining surface-based and space-based atmospheric CO_2 measurements, Journal ofGeophysical Research: Atmospheres, 125, https://doi.org/10.1029/2019JD032029, 2020.